Application of extended Mohr–Coulomb criterion to ductile fracture

Yuanli Bai · Tomasz Wierzbicki

Abstract The Mohr–Coulomb (M–C) fracture criterion is revisited with an objective of describing ductile fracture of isotropic crack-free solids. This criterion has been extensively used in rock and soil mechanics as it correctly accounts for the effects of hydrostatic pressure as well as the Lode angle parameter. It turns out that these two parameters, which are critical for characterizing fracture of geo-materials, also control fracture of ductile metals (Bai and Wierzbicki 2008; Xue 2007; Barsoum 2006; Wilkins et al. 1980). The local form of the M–C criterion is transformed/extended to the spherical coordinate system, where the axes are the equivalent strain to fracture $\bar{\varepsilon}_f$, the stress triaxiality η, and the normalized Lode angle parameter $\bar{\theta}$. For a proportional loading, the fracture surface is shown to be an asymmetric function of $\bar{\theta}$. A detailed parametric study is performed to demonstrate the effect of model parameters on the fracture locus. It was found that the M–C fracture locus predicts almost exactly the exponential decay of the material ductility with stress triaxiality, which is in accord with theoretical analysis of Rice and Tracey (1969) and the empirical equation of Hancock and Mackenzie (1976), Johnson and Cook

Y. Bai (✉) · T. Wierzbicki
Impact and Crashworthiness Laboratory, Massachusetts Institute of Technology, Cambridge, MA 02139, USA
e-mail: byl@alum.mit.edu

Present Address:
Y. Bai
General Electric Global Research Center, Niskayuna, NY, USA

(1985). The M–C criterion also predicts a form of Lode angle dependence which is close to parabolic. Test results of two materials, 2024-T351 aluminum alloy and TRIP RA-K40/70 (TRIP690) high strength steel sheets, are used to calibrate and validate the proposed M–C fracture model. Another advantage of the M–C fracture model is that it predicts uniquely the orientation of the fracture surface. It is shown that the direction cosines of the unit normal vector to the fracture surface are functions of the "friction" coefficient in the M–C criterion. The phenomenological and physical sound M–C criterion has a great potential to be used as an engineering tool for predicting ductile fracture.

1 Introduction

The Mohr–Coulomb (M–C) fracture criterion (Coulomb 1776; Mohr 1914) has been widely used in rock and soil mechanics (e.g. Zhao (2000); Palchik (2006)) and other relatively brittle materials (e.g. Lund and Schuh (2004)). This is a physically sound and simple fracture model. Fundamentals and applications of this model can be found in many textbooks, monographs and research papers. As a stress-based criterion, the Mohr–Coulomb model has good resolution for materials

that fail in the elastic range and/or under small strain plasticity, such as rock, soil, concrete and so on.

There have recently been several successful applications of this model for predicting fracture of ceramics under static and dynamic loading (Fossum and Brannon 2006). The M–C criterion is a special case of the Sandia GeoModel (Fossum and Brannon 2005). A unique feature of the M–C model is an explicit dependence on the Lode angle parameter, which is missing in almost all existing models of ductile fracture. The purpose of the present paper is to demonstrate the applicability of the M–C criterion to ductile fracture of uncracked bodies.

Meanwhile, the ductile fracture community took a different path. In search for a physically based fracture model, the mechanism of nucleation, growth and coalescence of void was identified and extensively studied. Due to fundamental work by McClintock (1968), Rice and Tracey (1969), Gurson (1975), Tvergaard and Needleman (1984), it was determined that ductile fracture is mostly affected by the hydrostatic pressure. Accordingly, the equivalent strain to fracture, which is a measure of material ductility, was made dependent on the first invariant of the stress tensor. The mixed stress–strain formulation of a fracture criterion is justifiable because, well into the plastic range, the resolution of strains is much larger than stresses, as explained in Fig. 1. Another feature of the Gurson-Tvergaard-Needleman (GTN) model (Tvergaard and Needleman 1984) is that it describes well the predominate tensile fracture, characterized by relatively high stress triaxiality, but fails to predict shear fracture. Attempts are currently underway to extend the void growth and coalescence model to describe shear fracture (Xue 2007; Nahshon and Hutchinson 2008). The M–C criterion is an extension of the maximum shear stress fracture criterion and therefore it is well poised to predict shear fracture.

In parallel with the "physically based" models of ductile fracture, a number of empirical fracture models have earned a permanent place in the literature (Cockcroft and Latham 1968; Hancock and Mackenzie 1976; Wilkins et al. 1980; Johnson and Cook 1985; Bao and Wierzbicki 2004; Wierzbicki and Xue 2005; Bai and Wierzbicki 2008). These models were based on extensive test programs on bulk material and/or sheets. One of the most comprehensive series of experiments involving tensile tests on unnotched and notched round bars, upsetting tests and shear tests was reported by
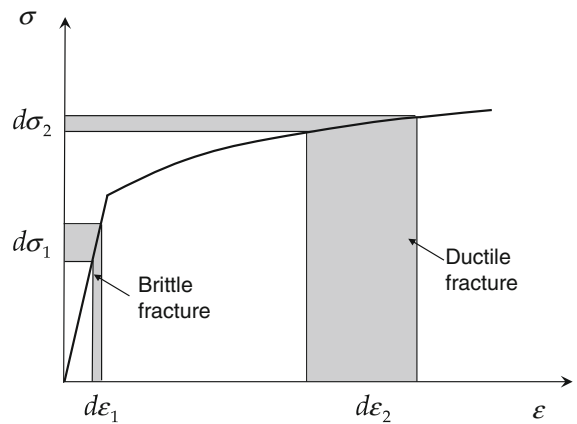
Fig. 1 Different resolution quality of strain and stress parameters: the stress parameters have good resolutions in the elastic region, and the strain parameters have good resolutions far in the plastic region

Bao (2003), Bao and Wierzbicki (2004). Even more recently Wierzbicki et al. (2005a), performed a series of fracture tests on specially designed butterfly specimens under combined tension/shear/compression loading. Results of bi-axial fracture tests on tubular specimens in the tension/torsion loading frame was published by Barsoum and Faleskog (2007), while Korkolis and Kyriakides (2008) studied fracture of 6260-T4 aluminum tubes subjected to internal pressure and axial tension or compression. All of these recent tests have proven that the material ductility depends on both stress triaxiality and the Lode angle parameter. These two effects are actually captured by the M–C model, as will be shown in the paper.

A particular case of Mohr–Coulomb criterion is the maximum shear stress criterion. It has been shown by Lee (2005) that the maximum shear stress criterion predicts well plane stress fracture for 2024-T351 aluminum alloy, see Fig. 2. A comparison of maximum shear stress criterion with other models was reported by Wierzbicki et al. (2005b). One main shortcoming of the maximal shear stress fracture criterion is the missing pressure dependence. The M–C criterion removes this shortcoming. To increase resolution of the ductile fracture prediction, the M–C criterion is transformed/extended to a strain-based representation under the assumption of monotonic loading. A parametric study is performed to get a better insight into this fracture model. The experimental results of two materials, 2024-T351 aluminum alloy (Bao 2003; Bao and Wierzbicki 2004; Wierzbicki et al. 2005b) and TRIP
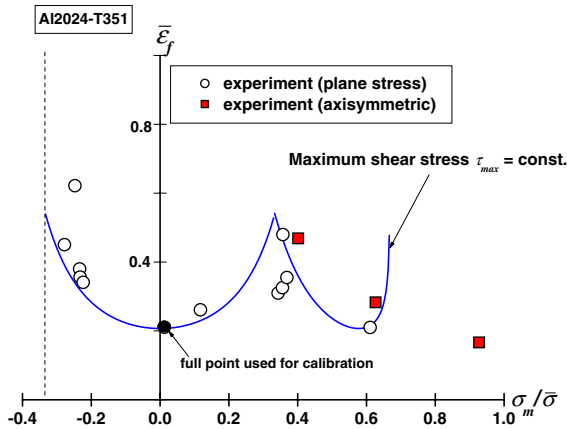
Fig. 2 Application of maximum shear stress fracture criterion to ductile fracture for plane stress condition (Lee 2005; Wierzbicki et al. 2005b)

RA-K40/70 steel sheets, are used to validate the new form of the Mohr–Coulomb criterion.

2 Characterization of the stress state

The three invariants of a stress tensor $[\sigma]$ are defined respectively by

$$p = -\sigma_m = -\frac{1}{3}\text{tr}([\sigma]) = -\frac{1}{3}(\sigma_1 + \sigma_2 + \sigma_3) \qquad (1)$$

$$q = \bar{\sigma} = \sqrt{\frac{3}{2}[S] : [S]}$$

$$= \sqrt{\frac{1}{2}\left[(\sigma_1 - \sigma_2)^2 + (\sigma_2 - \sigma_3)^2 + (\sigma_3 - \sigma_1)^2\right]} \qquad (2)$$

$$r = \left(\frac{9}{2}[S] \cdot [S] : [S]\right)^{1/3} = \left[\frac{27}{2}\det([S])\right]^{1/3}$$

$$= \left[\frac{27}{2}(\sigma_1 - \sigma_m)(\sigma_2 - \sigma_m)(\sigma_3 - \sigma_m)\right]^{1/3} \qquad (3)$$

where $[S]$ is the deviatoric stress tensor defined by,

$$[S] = [\sigma] + p[I], \qquad (4)$$

$[I]$ is the identity tensor and σ_1, σ_2 and σ_3 denote principal stresses. It is assumed that $\sigma_1 \geq \sigma_2 \geq \sigma_3$. Note that the parameter p is positive in compression, but σ_m is positive in tension. It is convenient to work with the dimensionless hydrostatic pressure η, defined by

$$\eta = \frac{-p}{q} = \frac{\sigma_m}{\bar{\sigma}}. \qquad (5)$$

The parameter η, often referred to as the triaxiality parameter, has been extensively used in the literature
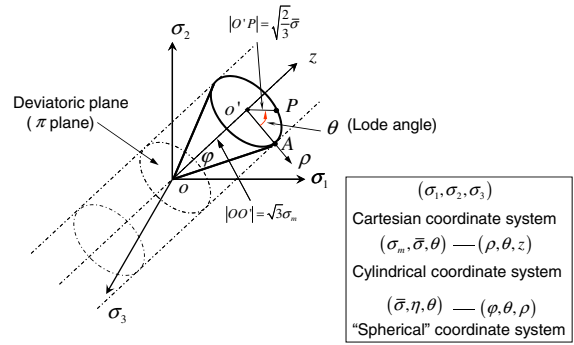
Fig. 3 Three types of coordinate system in the space of principal stresses

on ductile fracture (McClintock 1968; Rice and Tracey 1969; Hancock and Mackenzie 1976; Mackenzie et al. 1977; Johnson and Cook 1985; Bao 2003). The second important parameter is the Lode angle θ, which is related to the normalized third invariant ξ through

$$\xi = \left(\frac{r}{q}\right)^3 = \cos(3\theta). \qquad (6)$$

One can see that that the normalized third deviatoric stress invariant can be expressed in terms of the Lode angle θ (see Malvern (1969), Xu and Liu (1995), ABAQUS 2005; the derivation is also summarized in Sect. 3.1). Since the range of the Lode angle is $0 \leq \theta \leq \pi/3$, the range of ξ is $-1 \leq \xi \leq 1$. The geometrical representation of Lode angle is shown in Fig. 3.

As shown in Fig. 3, one can think of three types of coordinate systems to describe the stress state. The first is the Cartesian coordinate system $(\sigma_1, \sigma_2, \sigma_3)$, the second is the cylindrical coordinate system $(\sigma_m, \bar{\sigma}, \theta)$, and the third is the spherical coordinate system $(\bar{\sigma}, \eta, \theta)$. The equivalent stress $\bar{\sigma}$ is related to the equivalent strain $\bar{\varepsilon}$ through the strain hardening function of a material. The coordinate φ is related to the stress triaxiality η by the following equation,

$$\eta = \frac{\sigma_m}{\bar{\sigma}} = \frac{\sqrt{2}}{3}\cotan\varphi. \qquad (7)$$

Furthermore, the Lode angle can be normalized,

$$\bar{\theta} = 1 - \frac{6\theta}{\pi} = 1 - \frac{2}{\pi}\arccos\xi. \qquad (8)$$

So that the range of $\bar{\theta}$ is $-1 \leq \bar{\theta} \leq 1$. The parameter $\bar{\theta}$ will be called the Lode angle parameter hereinafter. Now, the direction of every stress vector (or loading condition) in the space of principal stresses can be characterized by the above defined set of parameters

$(\eta, \bar{\theta})$. It is easy to show (Wierzbicki and Xue 2005; Bai and Wierzbicki 2008) that $\bar{\theta} = 1$ corresponds to the axisymmetric tension, $\bar{\theta} = 0$ corresponds to the generalized shear (or plastic plane strain) loading condition, and $\bar{\theta} = -1$ corresponds to the axisymmetric compression or equi-biaxial tension. Special attention is given to the plane stress state. It was shown by Wierzbicki and Xue (2005), Bai and Wierzbicki (2008) that the plane stress condition, $\sigma_3 = 0$, uniquely relates the parameters η and ξ or $\bar{\theta}$ through

$$\xi = \cos(3\theta) = \cos\left[\frac{\pi}{2}(1-\bar{\theta})\right] = -\frac{27}{2}\eta\left(\eta^2 - \frac{1}{3}\right). \tag{9}$$

In this paper, the Mohr–Coulomb model will be reformulated in the spherical coordinate system.

3 Transformation of Mohr–Coulomb to the space of $(\bar{\varepsilon}_f, \eta, \bar{\theta})$

Consider a material element subjected to three principal stresses σ_1, σ_2, and σ_3. At an arbitrary cutting plane defined by the unit normal vector (v_1, v_2, v_3), the shear stress and the corresponding normal stress are given by

$$\tau = \sqrt{v_1^2 v_2^2 (\sigma_1 - \sigma_2)^2 + v_2^2 v_3^2 (\sigma_2 - \sigma_3)^2 + v_3^2 v_1^2 (\sigma_3 - \sigma_1)^2}, \tag{10}$$

$$\sigma_n = v_1^2 \sigma_1 + v_2^2 \sigma_2 + v_3^2 \sigma_3, \tag{11}$$

where the three components v_1, v_2 and v_3 are constrained by $v_1^2 + v_2^2 + v_3^2 = 1$.

The Mohr–Coulomb fracture criterion says that fracture occurs when the combination of normal stress and shear stress reach a critical value, according to

$$(\tau + c_1 \sigma_n)_f = c_2, \tag{12}$$

where c_1, c_2 are material constants. The constant c_1 is often referred to as a "friction" coefficient, and c_2 is shear resistance. The ranges of c_1 and c_2 are $c_1 \geq 0$ and $c_2 > 0$. In the limiting case of $c_1 = 0$, the M–C criterion reduces to the maximal shear stress criterion.

The applicability of the M–C criterion to capture ductile fracture will be shown in Sect. 8. In order to find on which cutting plane the M–C criterion will be met first, one must solve the following maximum value problem:

$$\begin{cases} \text{Max} \left\{ \sqrt{v_1^2 v_2^2 (\sigma_1 - \sigma_2)^2 + v_2^2 v_3^2 (\sigma_2 - \sigma_3)^2 + v_3^2 v_1^2 (\sigma_3 - \sigma_1)^2} \right. \\ \qquad \left. + c_1 \left(v_1^2 \sigma_1 + v_2^2 \sigma_2 + v_3^2 \sigma_3 \right) \right\} \\ \text{Subject to } v_1^2 + v_2^2 + v_3^2 = 1 \end{cases} \tag{13}$$

Recalling that $\sigma_1 \geq \sigma_2 \geq \sigma_3$, the solution of the maximum value problem using the Lagrangian multiplier technique is

$$\begin{cases} v_1^2 = \dfrac{1}{1+\left(\sqrt{1+c_1^2}+c_1\right)^2} \\ v_2^2 = 0 \\ v_3^2 = \dfrac{1}{1+\left(\sqrt{1+c_1^2}-c_1\right)^2} \end{cases}, \tag{14}$$

where v_1, v_2, and v_3 are direction cosines of maximum, intermediate, and minimum principal stresses, respectively. Substituting Eq. 14 into Eq. 12, the M–C criterion can be expressed in terms of principal stresses,

$$\left(\sqrt{1+c_1^2}+c_1\right)\sigma_1 - \left(\sqrt{1+c_1^2}-c_1\right)\sigma_3 = 2c_2, \tag{15}$$

provided that $\sigma_1 \geq \sigma_2 \geq \sigma_3$. The plane stress representation of the above fracture criterion is shown in Fig. 20. In view of enormous literature on the M–C criterion, the solution to the above maximum value problem must have been published earlier. However, the present authors were unable to find any reference on this topic. Here, only the final results are given. It should be noted that the orientation of the fracture plane depends only on the friction coefficient c_1, while the onset of fracture is controlled by both c_1 and c_2. In order to transform the Mohr–Coulomb criterion to the space of $(\bar{\varepsilon}_f, \eta, \bar{\theta})$, one needs to express principal stresses in terms of σ_m, η and θ. Similar transformation equations can be found, for example, in Malvern (1969). However, for the consistency of notation, the required transformation is derived here from the geometrical construction in Sect. 3.1.

3.1 Representation of the M–C criterion in terms of $\bar{\sigma}$, η and θ

The principal stresses and principal deviatoric stesses can be geometrically represented on the deviatoric plane (π plane), as shown in Fig. 4. Note that all the components are scaled because of the inclined angle between the deviatoric plane and the principal axis (see Fig. 3). From the geometrical construction, one can easily obtain the expressions of the deviatoric principal stresses in terms of $\bar{\sigma}$ and θ,
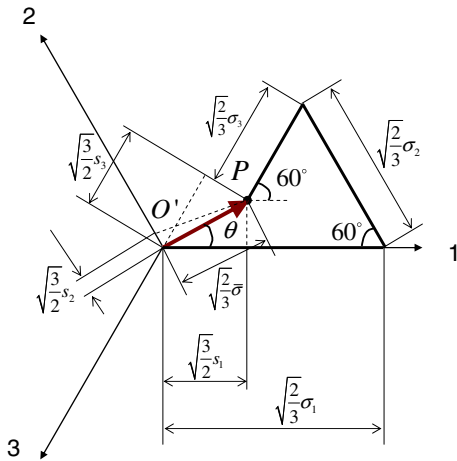
Fig. 4 Geometrical representation of principal stresses $(\sigma_1, \sigma_2, \sigma_3)$, deviatoric stresses (s_1, s_2, s_3), equivalent stress $(\bar{\sigma})$ and Lode angle (θ) on the deviatoric plane (π plane)

$$\begin{cases} \sqrt{\dfrac{3}{2}}s_1 = \sqrt{\dfrac{2}{3}}\bar{\sigma}\cos\theta \\[2mm] \sqrt{\dfrac{3}{2}}s_2 = \sqrt{\dfrac{2}{3}}\bar{\sigma}\cos\left(\dfrac{2}{3}\pi - \theta\right) \\[2mm] \sqrt{\dfrac{3}{2}}s_3 = \sqrt{\dfrac{2}{3}}\bar{\sigma}\cos\left(\dfrac{4}{3}\pi - \theta\right) \end{cases}$$

$$\Rightarrow \begin{cases} s_1 = \dfrac{2}{3}\bar{\sigma}\cos\theta \\[2mm] s_2 = \dfrac{2}{3}\bar{\sigma}\cos\left(\dfrac{2}{3}\pi - \theta\right) \\[2mm] s_3 = \dfrac{2}{3}\bar{\sigma}\cos\left(\dfrac{4}{3}\pi - \theta\right) \end{cases}. \qquad (16)$$

It should be noted that the constraint of deviatoric principal stresses,

$$s_1 + s_2 + s_3 = \frac{2}{3}\bar{\sigma}\left[\cos\theta + \cos\left(\frac{2}{3}\pi - \theta\right)\right.$$
$$\left. + \cos\left(\frac{4}{3}\pi - \theta\right)\right] = 0, \qquad (17)$$

is satisfied automatically. Using Eq. 16, one can express the three principal stresses in terms of σ_m, η and θ.

$$\begin{cases} \sigma_1 = \sigma_m + s_1 = \sigma_m + \frac{2}{3}\bar{\sigma}\cos\theta = \left[1 + \frac{2\cos\theta}{3\eta}\right]\sigma_m \\[2mm] \sigma_2 = \sigma_m + s_2 = \sigma_m + \frac{2}{3}\bar{\sigma}\cos\left(\frac{2}{3}\pi - \theta\right) \\[2mm] \quad = \left[1 + \frac{2\cos\left(\frac{2}{3}\pi - \theta\right)}{3\eta}\right]\sigma_m \\[2mm] \sigma_3 = \sigma_m + s_3 = \sigma_m + \frac{2}{3}\bar{\sigma}\cos\left(\frac{4}{3}\pi - \theta\right) \\[2mm] \quad = \left[1 + \frac{2\cos\left(\frac{4}{3}\pi - \theta\right)}{3\eta}\right]\sigma_m \end{cases} \qquad (18)$$

Since the range of Lode angle is $0 \leq \theta \leq \pi/3$, it can be proved that $\sigma_1 \geq \sigma_2 \geq \sigma_3$ is satisfied for the three principal stresses in Eq. 18. Using Eq. 18, one can also prove the relationship of the normalized third deviatoric invariant ξ and the Lode angle θ expressed earlier in Eq. 6. Also, the condition of plane stress (Eq. 9) can be easily proved by using the above transformation formulas.

Substituting Eq. 18 into Eq. 15, one can express the M–C criterion in terms of $\bar{\sigma}$, η and θ,

$$\bar{\sigma} = c_2\left[\sqrt{\frac{1 + c_1^2}{3}}\cos\left(\frac{\pi}{6} - \theta\right)\right.$$
$$\left. + c_1\left(\eta + \frac{1}{3}\sin\left(\frac{\pi}{6} - \theta\right)\right)\right]^{-1}. \qquad (19)$$

This fracture envelope forms a surface in the space of normalized stress invariants, which is also the "spherical" stress coordinate system.

3.2 Extended plasticity model

As explained in Fig. 1, the resolution of detecting the onset of ductile fracture is much better if a strain representation is used. Furthermore, fracture is a local phenomenon with large stress gradients. There is no easy way of measuring components of the stress tensor and evaluate $\bar{\sigma}$ directly from tests. This difficulty is overcome if the equivalent stress is expressed in terms of other measurable parameters.

The quadratic yield condition, on which the power type relation between the equivalent stress and the equivalent strain is based, $\bar{\sigma} = A\bar{\varepsilon}^n$, is not sufficient to predict correctly material yield strength and directions of plastic flow. Hosford (1972) proposed a non-quadratic yield function with one more parameter k,

$$2\bar{\sigma}_y^{2k} = (\sigma_1 - \sigma_2)^{2k} + (\sigma_2 - \sigma_3)^{2k} + (\sigma_3 - \sigma_1)^{2k}. \qquad (20)$$

Equation 20 reduces respectively to the von Mises yield condition for $k = 1$ and to the Tresca yield locus for $k \to \infty$. The actual value of the exponent $2k$ can be adjusted to test fit experimental data on biaxial testing. For example $2k = 8$ was quoted to fit the initial yield surface of a class of aluminum alloys. Further extension of the Hosford yield condition for isotropic and anisotropic solids and sheets can be found in the papers by Karafillis and Boyce (1993), Barlat et al. (2007).

Recent experimental results (Bai and Wierzbicki 2008; Yang et al. 2009; Gao et al. 2009) have shown that both the hydrostatic pressure and Lode angle parameter should be taken into account in metal plasticity. Bai and Wierzbicki (2008) proposed a generalized hardening rule with pressure and Lode angle dependence in the form,

$$\bar{\sigma} = A\bar{\varepsilon}^n \left[1 - c_\eta(\eta - \eta_\circ)\right] \left[c_\theta^s + (c_\theta^{ax} - c_\theta^s)\gamma\right], \quad (21)$$

$$c_\theta^{ax} = \begin{cases} 1 & \text{for } \bar{\theta} \geq 0 \\ c_\theta^c & \text{for } \bar{\theta} < 0 \end{cases}. \quad (22)$$

where A is a material constant, n is the strain hardening exponent, and c_η, $\eta_\circ$, c_θ^s and c_θ^c are parameters to describe both the pressure dependence and Lode angle dependence of the material plasticity. Altogether, there are six parameters defining the plasticity model. The parameter γ in Eq. 21 is related to the Lode angle parameter by

$$\gamma = \frac{\sqrt{3}}{2 - \sqrt{3}} \left[\sec\left(\theta - \frac{\pi}{6}\right) - 1\right]$$
$$= \frac{\sqrt{3}}{2 - \sqrt{3}} \left[\sec\left(\frac{\bar{\theta}\pi}{6}\right) - 1\right]. \quad (23)$$

Some limiting cases of the general yield function are obtained by suitably choosing model parameters. It is noted that by fixing the parameters $c_\theta^c = 1$ and $c_\eta = 0$, there is a close analogy between the non-quadratic Hosford yield function and the new representation of yield function in terms of $\bar{\sigma}$ and $\bar{\theta}$, Eq. 21. For example, $c_\theta^s = 1$ corresponds to the von-Mises yield condition; while $c_\theta^s = \sqrt{3}/2$ gives the Tresca yield condition. Thus, there is a one-to-one correspondence between the exponent k in Eq. 20 and parameter c_θ^s in Eq. 21. The presence of the parameter c_θ^c gives additional flexibility to the size and shape of the yield surface, as illustrated in Fig. 5.

3.3 Representation of the M–C criterion in terms of $\bar{\varepsilon}_f$, η and $\bar{\theta}$

Consider the case of a monotonic loading, and denote the equivalent stress and strain at the point of fracture by $\bar{\sigma}_f$ and $\bar{\varepsilon}_f$. Substituting Eq. 21 and Eq. 23 into Eq. 19, the Mohr–Coulomb fracture criterion is transformed from the stress-based form into the mixed space
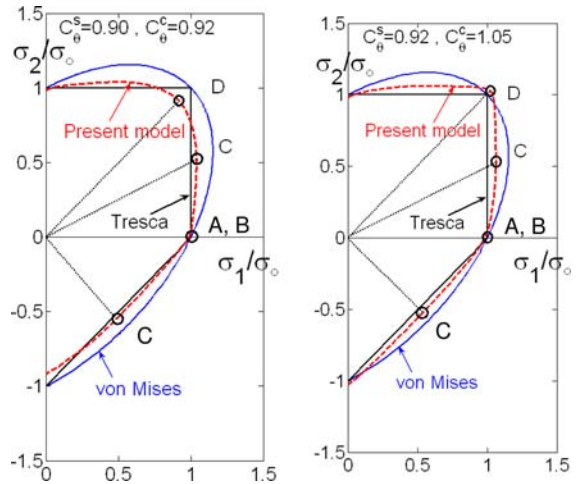
Fig. 5 Examples of yield loci for plane stress condition. (Here, the effect of hydrostatic pressure is deactivated, $c_\eta = 0$)

of $(\bar{\varepsilon}_f, \eta, \bar{\theta})$.

$$\bar{\varepsilon}_f = \left\{ \frac{A}{c_2} \left[1 - c_\eta(\eta - \eta_\circ)\right] \right.$$
$$\times \left[c_\theta^s + \frac{\sqrt{3}}{2 - \sqrt{3}}(c_\theta^{ax} - c_\theta^s)\left(\sec\left(\frac{\bar{\theta}\pi}{6}\right) - 1\right)\right]$$
$$\left. \left[\sqrt{\frac{1 + c_1^2}{3}} \cos\left(\frac{\bar{\theta}\pi}{6}\right) + c_1\left(\eta + \frac{1}{3}\sin\left(\frac{\bar{\theta}\pi}{6}\right)\right)\right] \right\}^{-\frac{1}{n}}. \quad (24)$$

A total of eight parameters $(A, n, c_\eta, \eta_\circ, c_\theta^s, c_\theta^c, c_1, c_2)$ need to be found, but only two have to be calibrated from fracture tests. If a von Mises yielding function is used ($c_\eta = 0$, $c_\theta^s = c_\theta^c = 1$), then Eq. 24 reduces to

$$\bar{\varepsilon}_f = \left\{ \frac{A}{c_2} \left[\sqrt{\frac{1 + c_1^2}{3}} \cos\left(\frac{\bar{\theta}\pi}{6}\right) + c_1\left(\eta + \frac{1}{3}\sin\left(\frac{\bar{\theta}\pi}{6}\right)\right)\right] \right\}^{-\frac{1}{n}}. \quad (25)$$

In the case of Tresca yield function ($c_\eta = 0$, $c_\theta^c = 1$, $c_\theta^s = \sqrt{3}/2$), and Eq. 24 reduces to

$$\bar{\varepsilon}_f = \left\{ \frac{A}{c_2} \left[\frac{\sqrt{1 + c_1^2}}{2} + c_1\frac{\sqrt{3}}{2}\sec\left(\frac{\bar{\theta}\pi}{6}\right)\left(\eta + \frac{1}{3}\sin\left(\frac{\bar{\theta}\pi}{6}\right)\right)\right] \right\}^{-\frac{1}{n}}. \quad (26)$$

In the above two limiting cases, the simplified plasticity model depends on only two parameters, A and n, which can be found from the same tests as the fracture tests. From the application point of view, the ease and practicality of the M–C criterion in terms of finding model parameters from experiments are obvious.
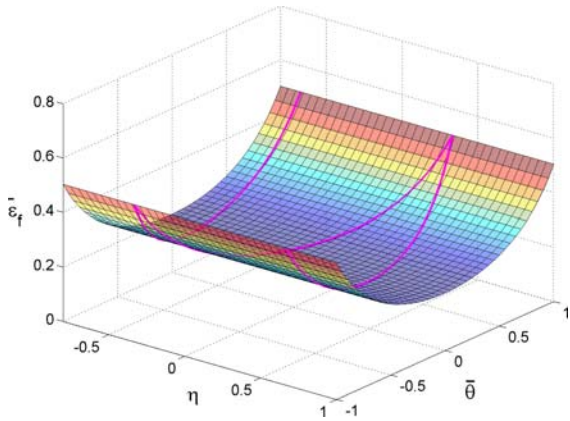
Fig. 6 3D geometry representation of maximum shear fracture criterion ($A = 740$ MPa, $n = 1/6$, $c_\eta = 0$, $c_\theta^s = c_\theta^c = 1$, $c_1 = 0.0$, and $c_2 = 330$ MPa). The *curve* on the surface represents the plane stress curve

Fig. 7 3D geometry representation of Mohr–Coulomb fracture model ($A = 740$ MPa, $n = 1/6$, $c_\eta = 0$, $c_\theta^s = c_\theta^c = 1$, $c_1 = 0.1$, and $c_2 = 330$ MPa)

4 A limiting case: maximum shear stress criterion

In the limiting case of $c_1 = 0$, the Mohr–Coulomb fracture criterion reduces to the maximum shear stress fracture criterion. For example, if the von Mises yield function is used, then Eq. 25 reduces to

$$\bar{\varepsilon}_f = \left[\frac{\sqrt{3}}{3} \frac{A}{c_2} \cos\left(\frac{\bar{\theta}\pi}{6}\right) \right]^{-\frac{1}{n}}, \qquad (27)$$

which is pressure independent. At the same time, the direction cosines of the fracture plane, defined by Eq. 14, are constant and equal to $\left(\frac{1}{\sqrt{2}}, 0, \frac{1}{\sqrt{2}}\right)$. A geometric representation of this criterion is shown in Fig. 6. The fracture locus depends only on the Lode angle parameter and forms a half tube in the space of $(\bar{\varepsilon}_f, \eta, \bar{\theta})$. The corresponding fracture locus for plane stress condition (Eq. 9) is a three-branch curve lying on the half tube. The projection of the plane stress fracture locus onto the plane of equivalent strain to fracture and the stress triaxiality is shown in Fig. 2, on which only two branches are plotted.

If the Tresca yielding condition is used, the maximum shear stress criterion, Eq. 26, reduces to the constant fracture strain criterion.

$$\bar{\varepsilon}_f = \left(\frac{A}{2c_2} \right)^{-\frac{1}{n}}. \qquad (28)$$

5 Representation of Mohr–Coulomb fracture criterion in 3D space of invariants

The new form of Mohr–Coulomb fracture model, Eq. 24, can be geometrically represented in the 3D space of $(\bar{\varepsilon}_f, \eta, \bar{\theta})$, see Fig. 7. Here, an example group of parameters is used: $A = 740$ MPa, $n = 1/6$, $c_\eta = 0$, $c_\theta^s = c_\theta^c = 1$, $c_1 = 0.1$, and $c_2 = 330$ MPa. The 3D fracture locus is seen to be a monotonic function of the stress triaxiality and an asymmetric function with respect to the Lode angle parameter $\bar{\theta}$.
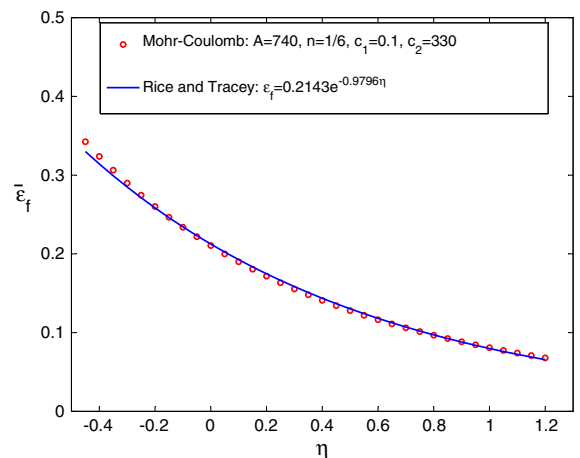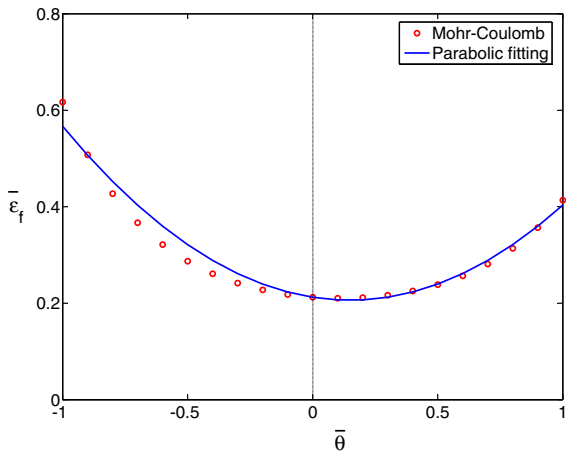

Fig. 8 Mohr–Coulomb criterion in the space of equivalent strain to fracture and stress triaxiality (assuming $\bar{\theta} = 0$)

5.1 Pressure dependence

If a von-Mises yielding function is used ($c_\eta = 0$, $c_\theta^s = c_\theta^c = 1$), and the Lode angle parameter $\bar\theta$ in Eq. 24 is fixed at a certain value, for example $\bar\theta = 0$, then Eq. 24 reduces to
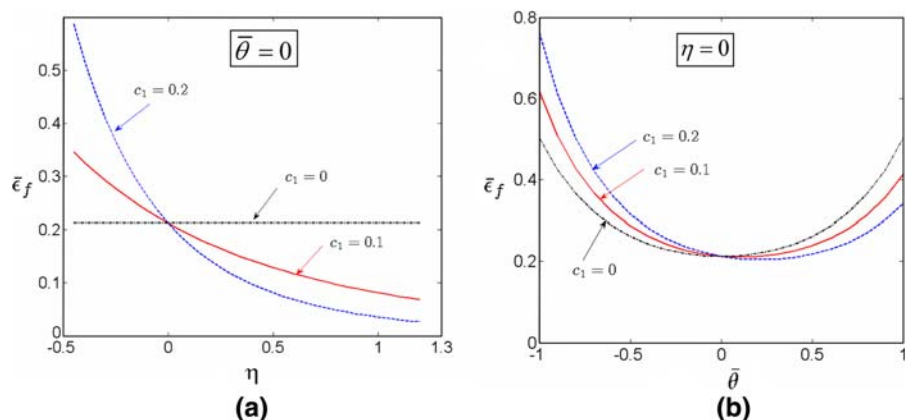
$$\bar\varepsilon_f = \left[\frac{A}{c_2} \left(\sqrt{\frac{1+c_1^2}{3}} + c_1\eta \right) \right]^{-\frac{1}{n}}. \qquad (29)$$

which is a nonlinear hyperbolic function of stress triaxiality η. An example plot of Eq. 29 is shown in Fig. 8. It is found that an exponential function $D_3 e^{-D_4\eta}$ fits Eq. 29 for a wide range of stress triaxiality. So, the Mohr–Coulomb criterion provides an interesting physical interpretation of the effect of stress triaxiality on ductile fracture, which is originally based on the theory of void growth (McClintock 1968; Rice and Tracey 1969). This is also in accord with the empirical results of Hancock and Mackenzie (1976), Johnson and Cook (1985).

5.2 Lode angle dependence

If the von-Mises yielding function is used again ($c_\eta = 0$, $c_\theta^s = c_\theta^c = 1$), and the stress triaxiality η in Eq. 24 is fixed at a certain value, for example $\eta = 0$, then Eq. 24 becomes

$$\bar\varepsilon_f = \left\{ \frac{A}{c_2} \left[\sqrt{\frac{1+c_1^2}{3}} \cos\left(\frac{\bar\theta\pi}{6}\right) + \frac{c_1}{3} \sin\left(\frac{\bar\theta\pi}{6}\right) \right] \right\}^{-\frac{1}{n}}. \qquad (30)$$

An example plot of Eq. 30 is shown in Fig. 9. A parabolic function controlled by three points, $\bar\varepsilon_f(\bar\theta = 1)$, $\bar\varepsilon_f(\bar\theta = 0)$ and $\bar\varepsilon_f(\bar\theta = -1)$, is used to fit the curve. It follows from Fig. 9 that a parabolic function provides a good functional dependence of the Lode angle parameter on ductile fracture. It should be noted that the minimum value of the function does not occur at $\bar\theta = 0$ but it is slightly shifted, which makes the 3D fracture locus an asymmetric function.

6 Parametric study

There are eight parameters (A, n, c_1, c_2, c_η, $\eta_\circ$, c_θ^s and c_θ^c) in the Mohr–Coulomb fracture criterion (see Eq. 24). In this section, a parameter study is performed to get a better understanding of new forms of Mohr–Coulomb criterion. In particular, some qualitative features of model parameters on the fracture locus are demonstrated. As a starting point, a combination of model parameters, $A = 740$ MPa, $n = 1/6$, $c_\eta = 0$,

Fig. 9 Mohr–Coulomb criterion on the space of equivalent strain to fracture and the Lode angle parameter (assuming $\eta = 0$)

Fig. 10 Effect of c_1 on the new form of the Mohr–Coulomb criteria

$\eta_\circ = 0$, $c_\theta^s = c_\theta^c = 1$, $c_1 = 0.1$ and $c_2 = 330$ MPa, is considered.

6.1 Effect of c_1

Keeping other parameters unchanged, the new form of the Mohr–Coulomb criterion is plotted for three values of c_1 ($c_1 = 0$, 0.1, and 0.2) on the same planes as those in Sects. 5.1 and 5.2, see Fig. 10. It is found that as c_1 increases, the fracture strain becomes more pressure dependent (see Fig. 10a), and the fracture locus becomes more asymmetric (see Fig. 10b). The limiting case $c_1 = 0$, which corresponds to the maximum shear stress criterion, implies a symmetric fracture locus with respect to Lode angle parameter $\bar{\theta}$.

6.2 Effect of c_2

Keeping other parameters unchanged, two values of c_2 are used to plot the new form of the Mohr–Coulomb criteria, see Fig. 11. It is found that the value of c_2 affect only the "height" of the fracture locus while the shape of the fracture locus is unchanged. A larger value of c_2 scales up the fracture locus.

6.3 Effect of A

Similarly, two values of A are used to plot the new form of the Mohr–Coulomb criteria, see Fig. 12. It is found that the parameter A has a similar effect as that of parameter c_2, but the effect of A on fracture locus is in the opposite direction of that of c_2. A larger value of A scales down the fracture locus. In other words, if a material gains more strength in the plastic range, then it loses some of its ductility. This property has been observed in many advanced high strength steels (Pfestorf 2005).

6.4 Effect of strain hardening exponent n

Again, two values of the strain hardening exponent, n, are used to plot the new form of the Mohr–Coulomb criteria, see Fig. 13. One obvious effect of the strain hardening exponent n is that it raises the fracture locus.

Three values of n ($\frac{1}{6}$, $\frac{1}{4}$ and $\frac{1}{2}$) are chosen in Fig. 14 to further demonstrate the effect of n. In Fig. 14a, all three curves are normalized with respect to $\bar{\varepsilon}_f(\eta = 0)$,

and in Fig. 14b, all curves are normalized with respect to $\bar{\varepsilon}_f(\bar{\theta} = 1)$. From Fig. 14a, one can see that a higher value of n decreases the pressure dependence of fracture locus. From Fig. 14b, one can see that a higher value of n decreases the dependence of fracture locus on the Lode angle parameter, which was first noted by Xue (2007) using the Stören and Rice necking criterion (Storen and Rice 1975).

6.5 Effect of c_η

Taking into account the pressure effect on material plasticity, for example, $c_\eta = 0.09$ and $\eta_\circ = 0$ with other parameters kept unchanged, a comparison of fracture locus is shown in Fig. 15. It is found that changing the parameter c_η has no effect on the Lode angle dependence of the fracture locus (see Fig. 15b), but increasing c_η will decrease the pressure dependence of the fracture locus (see Fig. 15a). In other words, if a material has more pressure dependence on plasticity, then it will have less pressure dependence on fracture. This result should also be further investigated experimentally on different materials.
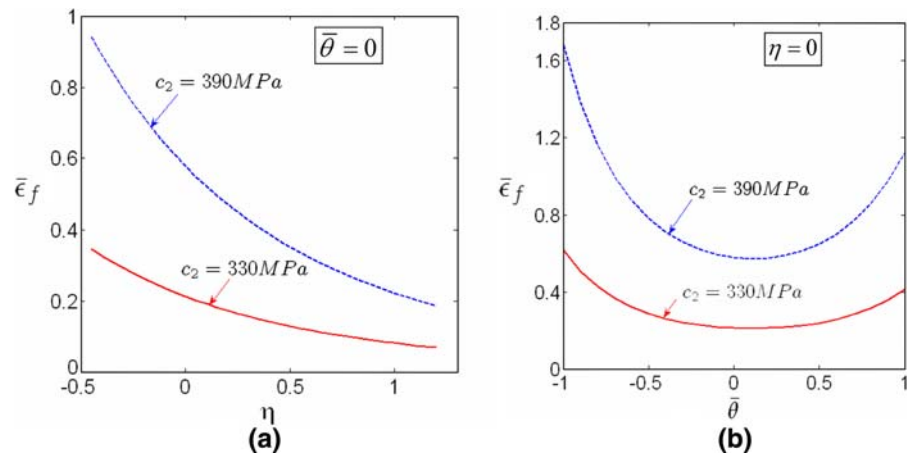
6.6 Effect of c_θ^s

Assuming $c_\theta^c = 1$, three values of c_θ^s (1.0, 0.93 and $\frac{\sqrt{3}}{2} = 0.866$) are used to plot the fracture locus, see Fig. 16. One can see that decreasing the parameter c_θ^s will raise the fracture locus (see Fig. 16a). On the other hand, decreasing c_θ^s will decrease the Lode dependence of the fracture locus (see Fig. 16b). In other words, if a material has stronger Lode dependence on plasticity, then it will have weaker Lode dependence on fracture. This point has been confirmed by comparing fracture data of two steels (1045 steel and DH36 steel), see (Bai et al. 2009). The 1045 steel has no Lode angle dependence on plasticity but exhibits a Lode angle dependence on fracture locus. On the other hand the DH36 exhibits a Lode angle dependence on plasticity but not on fracture.
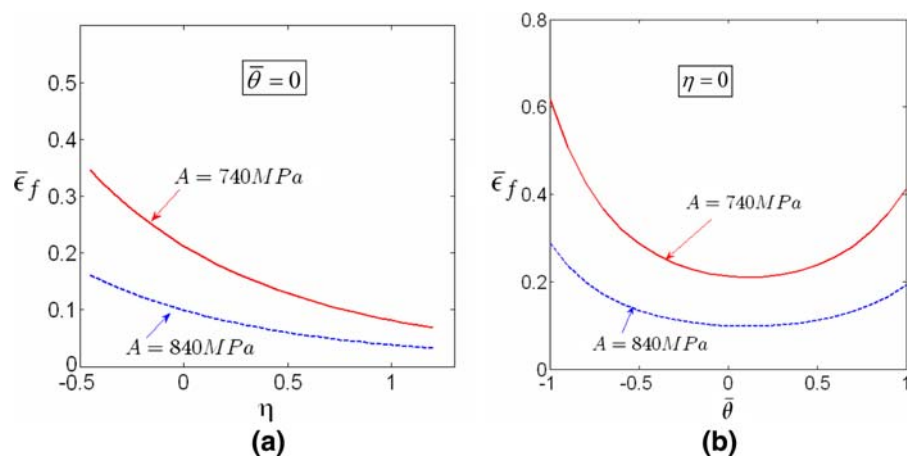
6.7 Effect of c_θ^c

In Eq. 21, the parameter, c_θ^c, controls the asymmetry of a yield surface, so this parameter will affect
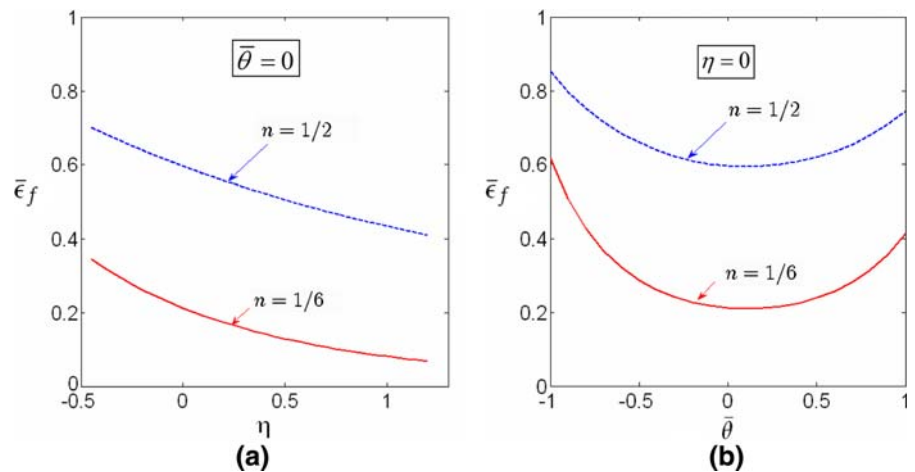
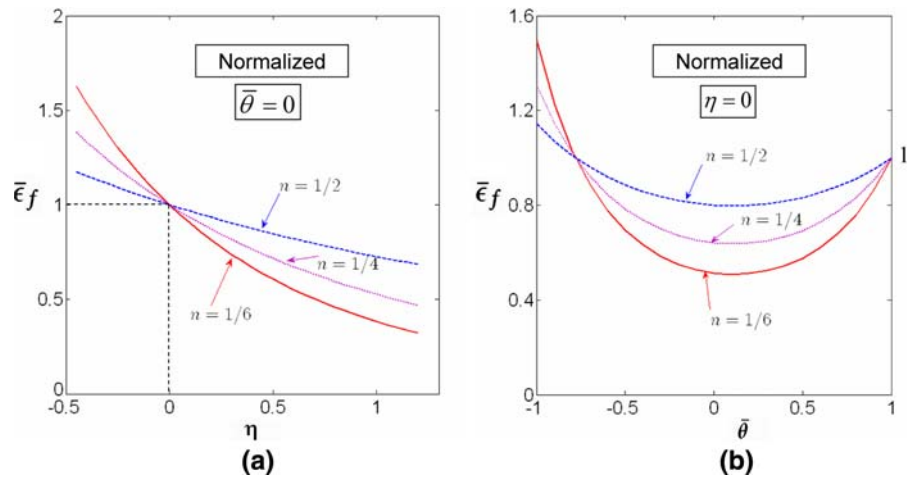**Fig. 11** Effect of c_2 on the new form of the Mohr–Coulomb criteria

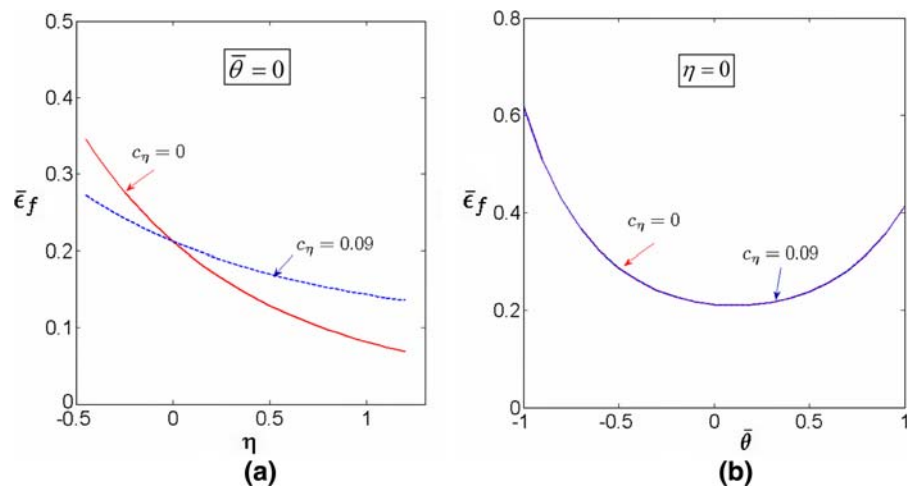**Fig. 12** Effect of A on the new form of the Mohr–Coulomb criteria

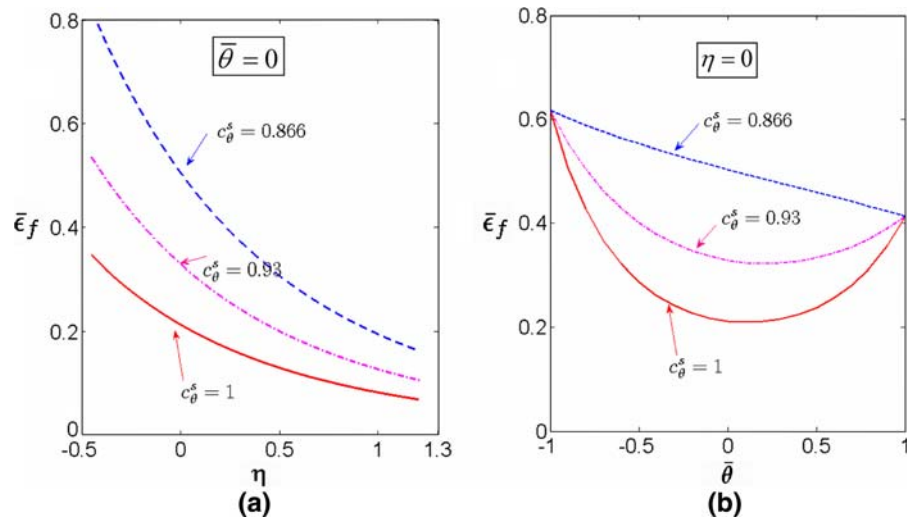**Fig. 13** Effect of n on the new form of the Mohr–Coulomb criteria

Fig. 14 A normalized plot to show the effect of n on the new form of the Mohr–Coulomb criteria


**Fig. 15** Effect of c_η on the new form of the Mohr–Coulomb criteria

Fig. 16 Effect of c_θ^s on the new form of the Mohr–Coulomb criteria. This parameter controls the amount of Lode angle dependence of the fracture locus

Fig. 17 Effect of c_θ^c on the new form of the Mohr–Coulomb criteria. This parameter controls the asymmetry of fracture locus with respect to the Lode angle parameter
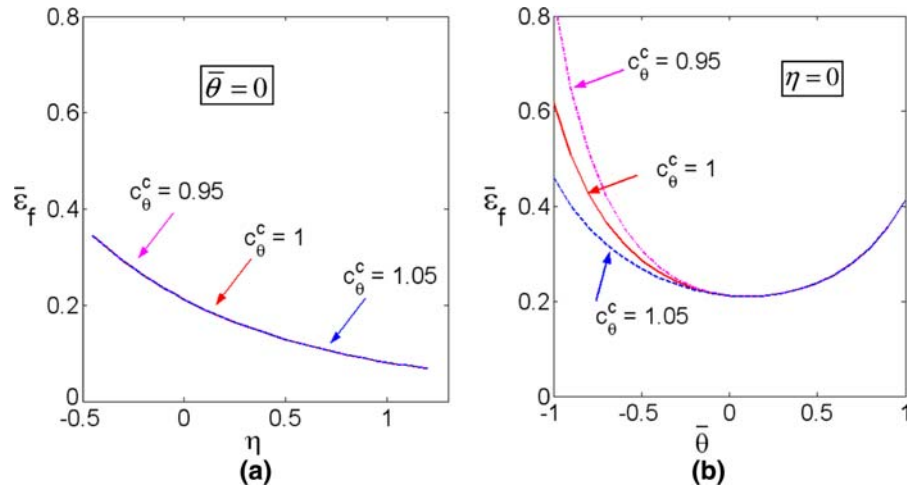
Fig. 18 A proposed shape of cutoff region of fracture one the plane of $(\eta, \bar{\theta})$ with $c_1 = 0.57$
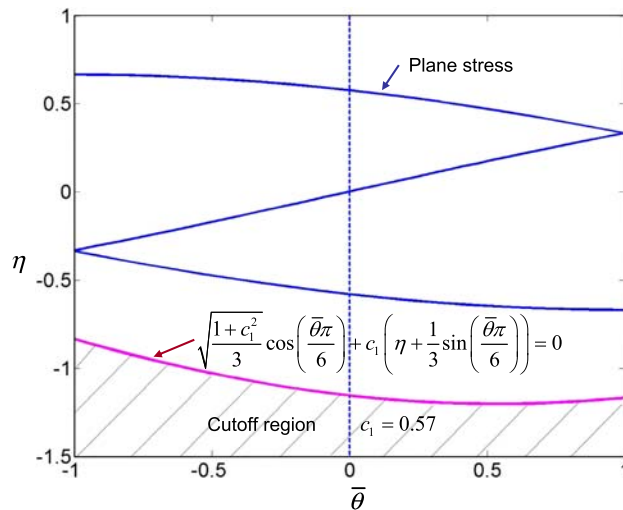

the asymmetry of material's fracture locus. Assuming $c_\theta^s = 1$, fracture loci with three values of c_θ^c (1.0, 0.95 and 1.05) are plot in Fig. 17. One can see that decreasing the parameter c_θ^c will raise the fracture strains at $\bar{\theta} = -1$ (see Fig. 17b), which changes the symmetry of the fracture locus. For some materials, fracture strain under equi-biaxial tension ($\bar{\theta} = -1$) is much higher than that of uni-axial tension ($\bar{\theta} = 1$), which would be controlled by the parameter c_θ^c. On the other hand, the parameter c_θ^c does not change the pressure dependence of fracture locus (see Fig. 16a). Referring to Sects. 6.4 and 6.6, it is found that the parameters, c_θ^s, c_θ^c and n, are the key parameters controlling the Lode angle effect on the fracture locus. This conclusion emphasizes the

importance of developing an accurate plasticity model to predict fracture.

6.8 Existence of a cutoff region

The existence of a cutoff value in the low stress triaxiality region has been revealed by Bao (2003), Bao and Wierzbicki (2005) and Teng (2004). Based on analysis of upsetting tests and Bridgman's tests (Bridgman 1952), Bao and Wierzbicki (2005) discovered that the cutoff value for fracture occurs at $\eta_{cutoff} = -\frac{1}{3}$. No fracture can occur below this critical value. Teng (2004) confirmed the importance of a cutoff value in high velocity impact simulation.
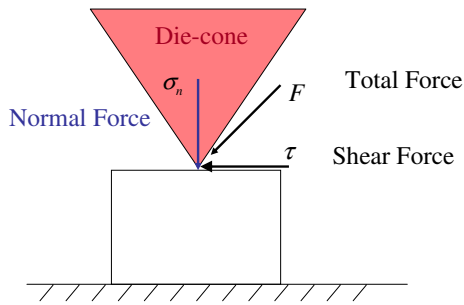
Fig. 19 A physical interpretation of existence cutoff region using the concept of die-cone in friction

Introducing the Lode angle parameter $\bar{\theta}$ into the ductile model, the cutoff region in the plane of the stress invariants $(\eta, \bar{\theta})$ of the 3D fracture locus appears automatically as a consequence of the M–C model. From Eq. 24, it is found that the fracture strain will go to infinity when the following condition is satisfied,

$$\sqrt{\frac{1+c_1^2}{3}} \cos\left(\frac{\bar{\theta}\pi}{6}\right) + c_1\left(\eta + \frac{1}{3}\sin\left(\frac{\bar{\theta}\pi}{6}\right)\right) \leq 0. \tag{31}$$

This cutoff region in the stress state plane $(\eta, \bar{\theta})$ is shown in Fig. 18 with a shaded area. In Fig. 18, an arbitrary value $c_1 = 0.57$ is assumed.

The above property of the cutoff region can be justified by revoking the physical concept of die-cone in the friction force, see Fig. 19. When the stress triaxiality η is less than a certain value, the vector of total force will be contained within the die-cone, under which condition slips will not occur during the material deformation. This gives an interesting physical interpretation of cutoff region using the Mohr–Coulomb criterion together with the concept of die-cone. However, "unrealistically" large values of the parameter c_1 would be needed in Eq. 31. Challenging tests should be designed and carried out in the future to explore this idea.

7 Crack directions in the plane stress and uni-axial stress

An important feature of M–C criterion is that it not only tells when a material point fails but also in which direction the material element cracks. In the general case, the crack plane is defined by Eq. 14. For the plane stress condition, it is convenient to consider a 2D representation of fracture planes, see Fig. 20. This picture was constructed taking $c_1 = 0.1$ as an example. The asym-

metric hexagon represents the locus of crack directions. For example, in the first quadrant, there will be slant fracture through thickness, but in the planar view, the crack forms perpendicular to the maximum principal stress. In the second and fourth quadrant, the through thickness crack is normal to the middle surface of a sheet, but follows an inclined planar direction. It is interesting to note that the planar vector of the crack direction is perpendicular to unit normal vector of the M–C fracture surface.

To simulate the crack propagation, the currently used technique in finite element simulation is based either on element deletion or element split along element edges. Neither of these two methods correctly simulates the boundary condition after a crack initiates, which is critical to predict the crack propagation, especially the slant fractures. It is suggested to use an extended element split technique in the spirit of an enriched FE shell element model suggested by Belytschko (for example, Areias and Belytschko (2005)). The direction of local element split surface will then follow from the M–C criterion. This is a technique requiring the joint efforts of both physical fracture modeling and finite element coding.

## 8 Experiment calibration and verification

8.1 A form of Mohr–Coulomb fracture locus proposed for application

Parameter study in Sect. 6 provides an insight understanding of the parameters in the Mohr–Coulomb fracture locus (Eq. 24). Since the effects of c_η and c_1 are similar in term of stress triaxiality, the term of pressure dependence on yield surface is neglected for simplicity. The following form of fracture locus is suggested for application.

$$\bar{\varepsilon}_f = \left\{ \frac{A}{c_2}\left[c_\theta^s + \frac{\sqrt{3}}{2-\sqrt{3}}\left(c_\theta^{ax} - c_\theta^s\right)\left(sec\left(\frac{\bar{\theta}\pi}{6}\right) - 1\right)\right] \right.$$
$$\left. \left[\sqrt{\frac{1+c_1^2}{3}}\cos\left(\frac{\bar{\theta}\pi}{6}\right) + c_1\left(\eta + \frac{1}{3}\sin\left(\frac{\bar{\theta}\pi}{6}\right)\right)\right] \right\}^{-\frac{1}{n}}, \tag{32}$$

where c_θ^{ax} is defined in Eq. 22. There are a total of six parameters $(A, n, c_1, c_2, c_\theta^s, c_\theta^c)$ that need to be found. The first two parameters, A and n, are parameters of material strain hardening, which can be calibrated from curve fitting of the stress–strain curve using power

Fig. 20 According to Mohr–Coulomb fracture criterion, a crack direction locus is proposed for plane stress conditions
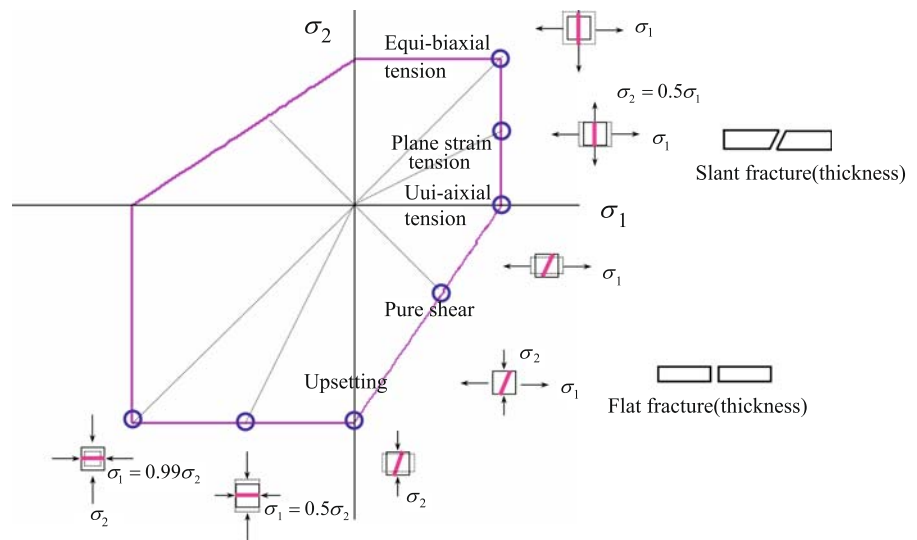
Fig. 21 Specimens used by Bao to calibrate the fracture locus for the wide range of stress triaxialtiy, see Table 1 for details
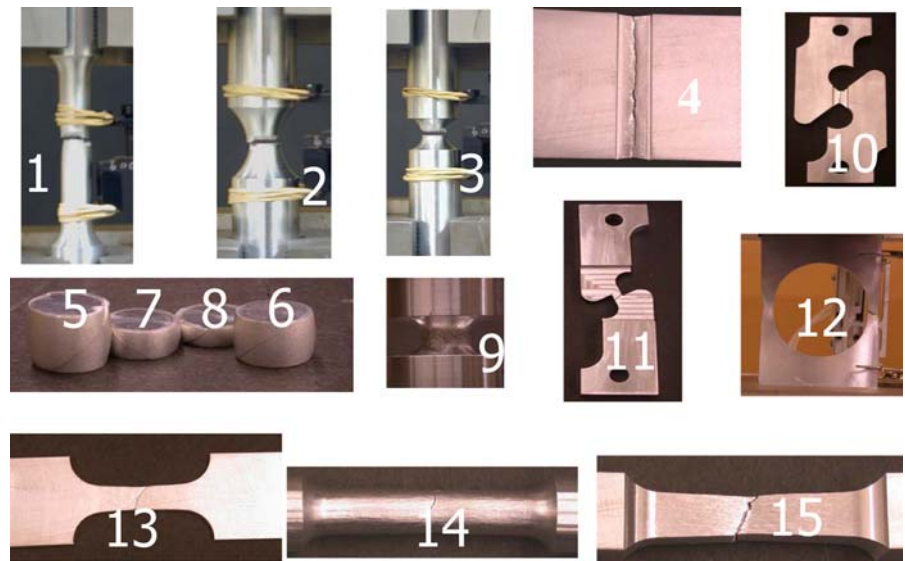
function. The two basic Mohr–Coulomb parameters, c_1 and c_2, need to be determined from material tests carried up to fracture. There are two additional parameters, c_θ^s and c_θ^c. The parameter c_θ^s controls the amount of Lode angle dependence, and the parameter c_θ^c affects the asymmetry of the fracture locus. Their default values are 1.0 if no additional test data are available. It should be noted that these two parameters, c_θ^s and c_θ^c, could be determined from careful plasticity tests and determination of the shape of the yield surface. Alternatively, one can leave those parameters undetermined in

the plasticity model and determine all four parameters $(c_1, c_2, c_\theta^s, c_\theta^c)$ from best fit of the fracture data points.

In the following two subsections, test data of two example materials are used to calibrate and verify the proposed Mohr–Coulomb fracture locus. One set of material data is taken from Bao and Wierzbicki's tests on aluminum alloy 2024-T351 (Bao 2003; Bao and Wierzbicki 2004; Wierzbicki et al. 2005b). The second set of material data on a TRIP steel sheet (RA-K40/70) from ThyssenKrupp was obtained by the present authors.

8.2 Example 1, Aluminum alloy 2024-T351

Bao and Wierzbicki (Bao 2003; Bao and Wierzbicki 2004; Wierzbicki et al. 2005b) performed a series of tests to calibrate the fracture locus of 2024-T351 aluminum alloy in a wide range of stress triaxiality, see Fig. 21. All the data from the 15 types of tests done by Bao and Wierzbicki are re-processed to calculate the Lode angle parameter $\bar{\theta}$, which was not introduced by Bao and Wierzbicki. Since in general the two stress state parameters are variable during the loading process, average values are used, according to the definitions given in Sect. 9. A list of the stress state parameters, η and $\bar{\theta}$, and the equivalent strain to fracture $\bar{\varepsilon}_f$ is shown in Table 1. The corresponding specimens of all the data points are labeled in Fig. 21. These tests, except test No.9 (where there were no obvious observed cracks), will be revisited using the new form of the Mohr–Coulomb criterion.

8.2.1 Plasticity

The parameters of the basic hardening curve, $A = 740$ MPa, $n = 0.15$, were found from the best fit of the stress–strain curve corresponding to the upsetting test (No. 6). In order to quantify the effect of Lode angle on plasticity (parameter c_θ^s and c_θ^c), axial-symmetric tension (test No. 1), axial-symmetric compression (test No. 6) and plane strain (test No. 4) experiments should be compared with each other, as described by Bai and Wierzbicki (2008). Such a comparison was performed by Bao (2003) showing that there is a very little Lode angle effect on plasticity. Therefore, for the purpose of the present analysis, the two parameters are set to unity ($c_\theta^s = c_\theta^c = 1$). This completes determination of plasticity constants.

8.2.2 Fracture

The M–C fracture criterion involves two basic material constants, so two tests are needed to calibrate this criterion. For that purpose, fracture test No. 6 and 10 of Table 1 are used. Substituting the experimental data (η_{av}, $\bar{\theta}_{av}$ and $\bar{\varepsilon}_f$) into Eq. 32, a set of two nonlinear algebraic equations for c_1 and c_2 are obtained. The solution of this system yields $c_1 = 0.0345$ and $c_2 = 338.6$ MPa. Now all six parameters in Eq. 32 have been determined. The plot of the resulting fracture locus is shown
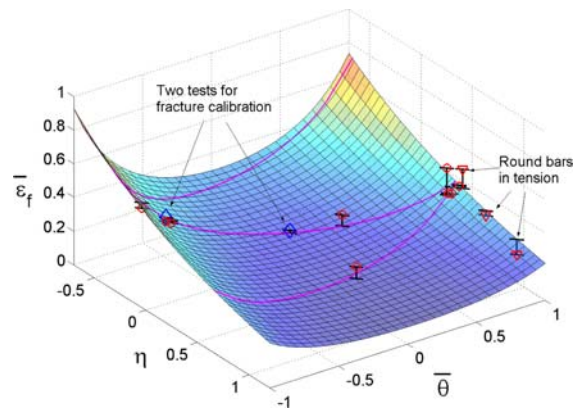

Fig. 22 3D geometric representation of Mohr–Coulomb fracture locus for 2024-T351 aluminum alloy. ($A = 740$ MPa, $n = 0.15$, $c_1 = 0.0345$, $c_2 = 338.6$ MPa, $c_\theta^s = c_\theta^c = 1.0$)

in Fig. 22. Tests No. 6 and 10, used for fracture calibration, are displayed as diamonds. The "half tube" surface passes exactly through those two points. Points corresponding to the remaining twelve tests are denoted by circles. They appear to be very close to the 3D surface, except for three points corresponding to unnotched and notched round bars. It has been shown by many investigators that the fracture in round bars in tension involves a mechanism of void growth and linkage. Clearly this is not well captured by the M–C fracture criterion. In other words, the M–C model describes shear type of fracture well but not fracture produced by void growth and linkage. It can be concluded that the M–C model is able to capture, with an engineering accuracy, shear fracture of 2024-T351 aluminum in a wide range of stress triaxiality and Lode angle parameter.

Most of the tests done by Bao and Wierzbicki were in plane stress condition, except for three round bars tensile tests (No. 1, 2 and 3). It follows from Eq. 9 that the plane stress data points lie on the "s"-shaped curve of plane stress condition. By substituting Eq. 9 into Mohr–Coulomb criterion, Eq. 32, the fracture locus of plane stress condition can be plotted on the plane of equivalent strain to fracture and the stress triaxiality (refer to Fig. 23). One can see that the fracture locus of plane stress consists of three half-cycles. This phenomenon was first revealed by Wierzbicki and Xue (Wierzbicki and Xue 2005) from a symmetric 3D fracture locus. The experimental data points used for calibration are marked in Fig. 23 by full circles. It is found that the calibrated Mohr–Coulomb criterion predicts the trends of experimental results very well. At the same

Table 1 A summary of Bao and Wierzbicki's test results on 2024-T351 aluminum, [experimental data after Bao (2003), Wierzbicki et al. (2005b)]

No.	Specimen description	η_{av}	$\bar{\theta}_{av}$	$\bar{\varepsilon}_f$
1	Smooth round bar, tension	0.4014	0.9992	0.4687
2	Round large notched bar, tension	0.6264	0.9992	0.2830
3	Round small notched bar, tension	0.9274	0.9984	0.1665
4	Flat grooved, tension	0.6030	0.0754	0.2100
5	Cylinder($d_o/h_o = 0.5$), compression	−0.2780	−0.8215	0.4505
6	Cylinder($d_o/h_o = 0.8$), compression	−0.2339	−0.6809	0.3800
7	Cylinder($d_o/h_o = 1.0$), compression	−0.2326	−0.6794	0.3563
8	Cylinder($d_o/h_o = 1.5$), compression	−0.2235	−0.6521	0.3410
9	Round notched, compression	−0.2476	−0.7141	0.6217
10	Simple shear	0.0124	0.0355	0.2107
11	Combination of shear and tension	0.1173	0.3381	0.2613
12	Plate with a circular hole	0.3431	0.9661	0.3099
13	Dog-bone specimen, tension	0.3570	0.9182	0.4798
14	Pipe, tension	0.3557	0.9286	0.3255
15	Solid square bar, tension	0.3687	0.9992	0.3551
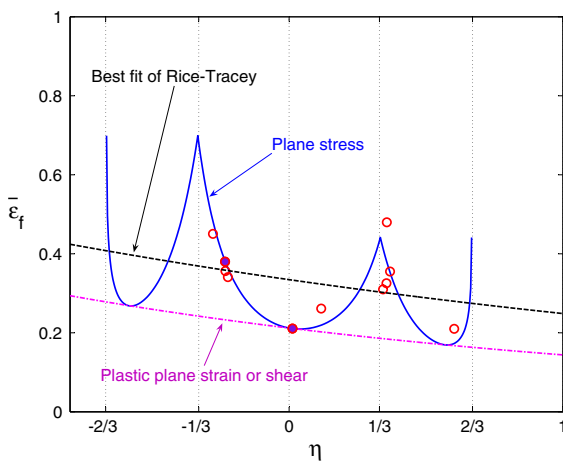
Fig. 23 Mohr–Coulomb fracture locus for 2024-T351 on the plane of equivalent strain to fracture and stress triaxiality. Only the test data under plane stress condition are plotted
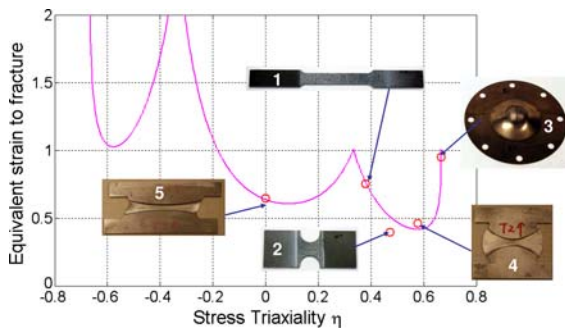
time the Rice–Tracey fracture model (Rice and Tracey 1969) can not predict the trend of plane stress fracture.

8.3 Example 2: TRIP RA-K40/70 steel sheet

The second example material is a TRIP steel sheet (RA-K40/70, or called TRIP690) provided by ThyssenKrupp Steel. The material comes in sheets, so all tests correspond to the plane stress condition. The material shows small amount of anisotropy in both plasticity and fracture properties. Dog-bone specimens were cut from three directions (0, 45 and 90 degrees) and tested under simple tension. The initial yield stresses are $\sigma_0 = 446.4$ MPa, $\sigma_{45} = 457.7$ MPa, and $\sigma_{90} = 455.5$ Mpa. Like the small difference in initial yielding, the subsequence material strain hardening in three directions are also very similar. The measured r-ratios in three directions are $r_0 = 0.79$, $r_{45} = 0.97$, and $r_{90} = 1.02$, which shows some material anisotropy in the plastic flow. These tension tests were carried all way to fracture, the measurement of area reductions at fracture cross-sections gave estimations of the equivalent fracture strains, which are

Table 2 A summary of test results on a TRIP steel

No.	Specimen description	η_{av}	$\bar{\theta}_{av}$	$\bar{\varepsilon}_f$
1	Dog-bone, tension	0.379	1.0	0.751
2	Flat specimen with cutouts, tension	0.472	0.4960	0.394
3	Disk specimen, equi-biaxial tension	0.667	−0.921	0.950
4	Butterfly specimen1, tension	0.577	0.0	0.460
5	Butterfly specimen2, simple shear	0.0	0.0	0.645

Fig. 24 Mohr–Coulomb fracture locus for a TRIP steel sheet on the plane of equivalent strain to fracture and stress triaxiality. ($A = 1275.9$ MPa, $n = 0.2655$, $c_1 = 0.12$, $c_2 = 720$ MPa, $c_\theta^s = 1.095$, $c_\theta^c = 1.0$)

$\bar{\varepsilon}_{f,0} = 0.703$, $\bar{\varepsilon}_{f,45} = 0.754$, and $\bar{\varepsilon}_{f,90} = 0.744$. One can see that the difference of fracture properties in three directions is also small. In this paper, materials are assumed to be isotropic. For simplicity, the plasticity of the TRIP steel sheet are described by an power hardening curve, $\bar{\sigma} = A\varepsilon^n = 1275.9\bar{\varepsilon}^{0.2655}$ MPa.

In total, five types of specimens are used for fracture calibration: dog-bone specimen, flat specimen with cutouts, punch test, butterfly specimen in tension and butterfly specimen in simple shear. Similarly, the average value of two stress state parameters ($\eta, \bar{\theta}$) are calculated from the numerical simulation using shell elements. A detail experimental and simulation results of those tests are described in the reference (Bai et al. 2008). A summary of the stress state parameters, η and $\bar{\theta}$, and the equivalent strain to fracture $\bar{\varepsilon}_f$ is shown in Table 2. The corresponding specimens of the data points are labeled in Fig. 24.

The first two parameters in the fracture locus (Eq. 32) are determined from the material plasticity, $A = 1275.9$ MPa and $n = 0.2655$. The remaining four parameters ($c_1, c_2, c_\theta^s, c_\theta^c$) are found from the best fit of equivalent strain to fracture for all five fracture tests. An approach of parameter optimization using Matlab code was described in reference (Bai and Wierzbicki 2008). Utilizing the same approach, the remaining four parameters are found as: $c_1 = 0.12$, $c_2 = 720$ MPa, $c_\theta^s = 1.095$, $c_\theta^c = 1.0$. A comparison of test results with the calibrated M–C criterion is shown in Fig. 24. Again, the M–C criterion was able to capture all features of the fracture locus of metal sheets.

9 Damage evolution rule

Besides the fracture locus, discussed extensively in the preceding section, the rule of damage evolution is an integral part of the fracture predictive technique. The fracture locus is defined under monotonic loading conditions, so a linear incremental relationship is assumed here between the damage indicator, D, and the equivalent plastic strain $\bar{\varepsilon}_p$,

$$D\left(\bar{\varepsilon}_p\right) = \int_0^{\bar{\varepsilon}_p} \frac{d\bar{\varepsilon}_p}{f\left(\eta, \bar{\theta}\right)}, \tag{33}$$

where the stress direction parameters, $\eta(\bar{\varepsilon}_p)$, and $\bar{\theta}(\bar{\varepsilon}_p)$, are unique functions of the equivalent plastic strain. A material element is considered to fail when the limit of ductility is reached, $\bar{\varepsilon}_p = \bar{\varepsilon}_f$, so that $D(\bar{\varepsilon}_f) = D_c = 1$. In the limiting case (for example proportional loading), when the parameters ($\eta, \bar{\theta}$) are constant over the loading cycle, Eq. 33 can be integrated to give

$$\bar{\varepsilon}_f = f\left(\eta, \bar{\theta}\right) = \hat{\varepsilon}_f\left(\eta, \bar{\theta}\right), \tag{34}$$

which reduces to the 3D fracture locus $\hat{\varepsilon}_f\left(\eta, \bar{\theta}\right)$. The best tests for calibration are the ones in which the stress parameters η and $\bar{\theta}$ are held constant. This is the case with the equi-biaxial punch test (No. 3 in Fig. 24), the shear test (No. 5), and to a certain extent with the flat notched specimens (No. 2) (Beese et al. 2009). In the general case of variable stress parameters, the integral representation of the fracture criterion must be used.

The functions, $\eta(\bar{\varepsilon}_p)$ and $\bar{\theta}(\bar{\varepsilon}_p)$, are known from the numerical simulation of the tests, and the equivalent strain to fracture $\bar{\varepsilon}_f$ is determined from inverse method of mapping the measured displacement to fracture into the calculated strain to fracture. Alternatively, fracture strains can be measured directly by an optical measurement system and the stress invariants can be calculated from a suitable plasticity model (Dunand and Mohr 2009). Then the unknown fracture parameters c_1, c_2, c_θ^s, and c_θ^c can be determined by minimizing the residue R defined by Eq. 35,

$$R = \int_0^{\bar{\varepsilon}_f} \frac{d\bar{\varepsilon}_p}{f\left(\eta, \bar{\theta}\right)} - 1. \tag{35}$$

Yet, the first method in which the equivalent strain to fracture is found directly from measurements and the values of stress triaxiality and Lode angle parameter are constant and known beforehand is by far superior.

In these cases, fracture calibration bypasses the need for a plasticity model which may introduce additional errors.

A linear incremental dependence of the damage function $D\left(\bar{\varepsilon}_p\right)$ on the equivalent plastic strain (Eq. 33) was shown to work well for monotonic loading. In the case of reverse straining or more complicated loading paths, a nonlinear incremental rule must be considered, as proposed by Bai (2008).

10 Discussion and conclusion

In this paper, the transformation formulas between the principal stresses and the stress state parameters (the stress triaxiality η and the Lode angle parameter $\bar{\theta}$) are derived. For monotonic loading conditions, the Mohr–Coulomb criterion is transformed from a local representation in terms of a shear stress and a normal stress, to the mixed strain-stress representation of $(\bar{\varepsilon}_f, \eta, \bar{\theta})$. The corresponding fracture locus of the Mohr–Coulomb criterion is shown to be described by a monotonically decreasing function of the stress triaxiality coupled with an asymmetric function of Lode angle parameter. A parametric study on the new form of the Mohr–Coulomb criterion was performed and the results are summarized as follows.

- Increasing the friction parameter c_1 increases both the dependence of fracture locus on pressure and the asymmetry of the fracture locus.
- Increasing the shear resistance parameter c_2 shifts the fracture locus upward without changing its shape.
- Increasing the amplitude of the power hardening law, parameter A, shifts the fracture locus down, but its shape remains the same. In other words, increasing the material's strength will decrease its ductility.
- Increasing the power exponent n shifts the fracture locus upward, but decreases both the pressure dependence and the Lode angle dependence of the fracture locus. In other words, less strain hardening materials will have more pressure and Lode angle dependence on fracture.
- Increasing the parameter c_η will decrease the pressure dependence of the fracture locus, but leave no effect on the shape of the fracture locus.
- Decreasing the parameter c_θ^s will increase the whole height of the fracture locus, and decrease the effect of Lode angle on the fracture locus. In other words,

if a material exhibits more Lode dependence on plasticity, then it has less Lode dependence on fracture, and vice versa.
- Decreasing the parameter c_θ^c will increase the fracture strains under axial symmetric compression conditions ($\bar{\theta} = -1$), which controls the asymmetry of the fracture locus.
- There exists a cutoff region on the stress state plane $(\eta, \bar{\theta})$, see Eq. 31, where fracture will not occur.

Bao and Wierzbicki's experimental results on 2024-T351 aluminum alloy are revisited using the new form of the Mohr–Coulomb criterion. Using two types of test to calibrate the basic Mohr–Coulomb parameters, the model predicts the remaining nine tests with good accuracy, especially for plane stress fracture. While the Mohr–Coulomb criterion predicts most of the shearing dominated fracture well, there are still some limitations of this fracture criterion. For example, it does not provide a good prediction of the fracture of round bars in tension, which satisfy the axial symmetry condition. At the same time, fracture in upsetting tests occurs at the equatorial region of the outer surface. This is a plane stress fracture, and it is predicted well by the M–C criterion.

As a second example, the test results on one type of advanced high strength steel, TRIP RA-K40/70 steel sheet, are provided to demonstrate the applicability of the proposed M–C criterion to metal sheets. The TRIP steel sheet shows small amount of anisotropy. It should be noted that the current M–C criterion assumes material isotropy, and it should be further extended to describe the fracture anisotropy, which is the on-going research.

The M–C criterion predicts not only crack initiation sites but also crack directions. Providing a given material element crack direction in conjunction with the arbitrary element splitting technique can predict crack path with greater accuracy. With the M–C criterion's clear and simple physical meaning, this ductile fracture model has great potential for many engineering applications.

References

ABAQUS (2005) User's manual, version 6.5, Hilbbit, Karlsson and Sorensen Inc.

Areias PMA, Belytschko T (2005) Analysis of three-dimensional crack initiation and propagation using the extended finite element method. Int J Numer Methods Eng 63: 760–788

Bai Y (2008) Effect of loading history on necking and fracture. PhD thesis, Massachusetts Institute of Technology, 2008

Bai Y, Wierzbicki T (2008) A new model of metal plasticity and fracture with pressure and lode dependence. Int J Plast 24(6):1071–1096

Bai Y, Teng X, Wierzbicki T (2009) On the application of stress triaxiality formula for plane strain fracture testing. J Eng Mater Technol 131(2), April 2009

Bai Y, Luo M, Li Y, Wierzbicki T (2008) Calibration of TRIP steel sheet (RA-K40/70) for fracture. Technical report, Impact and Crashworthiness Laboratory, Massachusetts Institute of Technology, Cambridge, MA

Bao Y (2003) Prediction of ductile crack formation in uncracked bodies. PhD thesis, Massachusetts Institute of Technology

Bao Y, Wierzbicki T (2004) On fracture locus in the equivalent strain and stress triaxiality space. Int J Mech Sci 46(1): 81–98

Bao Y, Wierzbicki T (2005) On the cut-off value of negative triaxiality for fracture. Eng Fract Mech 72(7):1049–1069

Barlat F, Yoon JW, Cazacu O (2007) On linear transformations of stress tensors for the description of plastic anisotropy. Int J Plast 23(5):876–896

Barsoum I (2006) Ductile failure and rupture mechanisms in combined tension and shear. PhD thesis, Royal Institute of Technology (KTH), Stockholm, Sweden

Barsoum I, Faleskog J (2007) Rupture mechanisms in combined tension and shear—experiments. Int J Solids Struct 44(6):1768–1786

Beese A, Luo M, Li Y, Bai Y, Wierzbicki T (2009) Partially coupled anisotropic fracture model for sheets. submitted to Engineering Fracture Mechanics for publication

Bridgman PW (1952) Studies in large plastic flow and fracture. McGraw-Hill, New York

Cockcroft MG, Latham DJ (1968) Ductility and the workability of metals. J Inst Met 96:33–39

Coulomb C (1776) Essai sur une application des regles des maximis et minimis a quelues problemes de statique relatifs a l'6architecture. Mem Acad Roy des Sci

Dunand M, Mohr D (2009) Determination of (multiaxial) ductile fracture properties of trip steel sheets using notched tensile specimens, report 193. Technical report, Impact and Crashworthiness Laboratory, Massachusetts Institute of Technology, Cambridge, MA

Fossum A, Brannon R (2005) The sandia geomodel: theory and user's guide. Technical report, Sandia National Laboratories, Albuquerque, NM and Livermore, CA

Fossum A, Brannon R (2006) On a viscoplastic model for rocks with mechanism-dependent characteristic times. Acta Geotechnica 1:89–106

Gao X, Zhang T, Hayden M, Roe C (2009) Effects of the stress state on plasticity and ductile failure of an aluminum 5083 alloy. Int J Plast 25(12): 2366–2382

Gurson AL (1975) Plastic flow and fracture behavior of ductile materials incorporating void nucleation, growth and interaction. PhD thesis, Brown University

Hancock JW, Mackenzie AC (1976) On the mechanisms of ductile failure in high-strength steels subjected to multi-axial stress-states. J Mech Phys Solids 24(2–3):147–160

Hosford W (1972) A generalized isotropic yield criterion. J Appl Mech 39:607

Johnson GR, Cook WH (1985) Fracture characteristics of three metals subjected to various strains, strain rates, temperatures and pressures. Eng Fract Mech 21(1):31–48

Karafillis AP, Boyce MC (1993) A general anisotropic yield criterion using bounds and a transformation weighting tensor. J Mech Phys Solids 41(12):1859–1886

Korkolis YP, Kyriakides S (2008) Inflation and burst of anisotropic aluminum tubes for hydroforming applications. Int J Plast 24(3):509–543

Lee Y-W (2005) Fracture prediction in metal sheets. PhD thesis, Massachusetts Institute of Technology

Lund A, Schuh C (2004) The mohr-coulomb criterion from unit shear processes in metallic glass. Intermetallics 12(10–11): 1159–1165

Mackenzie AC, Hancock JW, Brown DK (1977) On the influence of state of stress on ductile failure initiation in high strength steels. Eng Fract Mech 9(1):167–168

Malvern LE (1969) Introduction to the mechanics of a continuous medium. Prentice-Hall, Inc., Englewood Cliffs

McClintock FA (1968) A criterion of ductile fracture by the growth of holes. J Appl Mech 35:363–371

Mohr O (1914) Abhandlungen aus dem Gebiete der Technischen Mechanik (2nd ed). Ernst, Berlin

Nahshon K, Hutchinson JW (2008) Modification of the Gurson model for shear failure. Eur J Mech A/Solids 27(1): 1–17

Palchik V (2006) Application of mohr-coulomb failure theory to very porous sandy shales. Int J Rock Mech Mining Sci 43(7):1153–1162

Pfestorf M (2005) The application of multiphase steel in the body-in white. In Great designs in 2005 steel seminar presentations

Rice JR, Tracey DM (1969) On the ductile enlargement of voids in triaxial stress fields. J Mech Phys Solids 17:201–217

Storen S, Rice JR (1975) Localized necking in thin sheets. J Mech Phys Solids 23(6):421–441

Teng X (2004) High velocity impact fracture. PhD thesis, Massachusetts Institute of Technology

Tvergaard V, Needleman A (1984) Analysis of the cup-cone fracture in a round tensile bar. Acta Materialia 32:157–169

Wierzbicki T, Xue L (2005b) On the effect of the third invariant of the stress deviator on ductile fracture. Technical report, Impact and Crashworthiness Laboratory, Massachusetts Institute of Technology, Cambridge, MA

Wierzbicki T, Bao Y, Bai Y (2005a) A new experimental technique for constructing a fracture envelope of metals under multi-axial loading. Proceedings of the 2005 SEM annual conference and exposition on experimental and applied mechanics. pp 1295–1303

Wierzbicki T, Bao Y, Lee Y-W, Bai Y (2005b) Calibration and evaluation of seven fracture models. Int J Mech Sci 47(4–5): 719–743

Wilkins ML, Streit RD, Reaugh JE (1980) Cumulative-strain-damage model of ductile fracture: simulation and prediction of engineering fracture tests, ucrl-53058. Technical report, Lawrence Livermore Laboratory, Livermore, California

Xu B, Liu X (1995) Applied mechanics: elasticity and plasticity. Tsinghua University Press, Beijing

Xue L (2007) Ductile fracture modeling—theory, experimental investigation numerical verification. PhD thesis, Massachusetts Institute of Technology

Yang F, Sun Q, Hu W (2009) Yield criterions of metal plasticity in diffierent stress states. Acta Metallurgica Sinica (English Letters). 22(2):123–130

Zhao J (2000) Applicability of mohr-coulomb and hoek-brown strength criteria to the dynamic strength of brittle rock. Int J Rock Mech Mining Sci 37(7):1115–1121